PAPER

Exclusive production of acetone using a copper nanoparticle anchored LSCO perovskite electrocatalyst: cell design and metal–support interaction governed electrocatalysis†

Shikha Dhakar,[a] Rishabh Kumar,[a] Rudranarayan Khatua,[a] Rahul Mitra,[b]
Rajashri R. Urkude,[c] Biplab Ghosh,[c] Anirban Mondal, [ID] [a] Krishanu Biswas[b] and
Sudhanshu Sharma [ID] *[a]

This study explores the enhancement of electrochemical CO_2 reduction (CO_2ER) using a novel Cu nanoparticle decorated $La_{0.8}Sr_{0.2}CoO_3$ (LSCO) perovskite catalyst. The synthesized Cu/LSCO catalyst exhibits exceptional activity and selectivity for acetone production. A systematic variation in Cu loading revealed a non-linear trend in performance: faradaic efficiency (FE) increased from ~40% for Cu 10/LSCO to a maximum of ~93.7% for Cu 20/LSCO but significantly dropped to 7.5% for Cu 30/LSCO. Cu 20/LSCO also delivered a partial current density of −20.28 mA cm^{-2}, making it the most efficient composition. This behavior highlights the importance of optimal Cu loading, where enhanced nanoparticle dispersion and strong metal–support interaction (MSI) result in greater active site availability and improved catalytic performance. In contrast, excessive Cu loading leads to particle agglomeration, and diminished CO_2ER activity. Cu 20/LSCO also exhibited stable performance over 40 000 seconds, demonstrating its potential for prolonged CO_2 electroreduction and highlighting its viability for sustainable CO_2 conversion in renewable energy applications. X-ray absorption spectroscopy (XAS) analysis confirmed the oxidation state and local coordination environment of Cu, providing critical mechanistic insight into the observed performance trend and the role of MSI. The Cu/LSCO catalyst, enhanced by metal–support interaction (MSI) along with the cell geometry, is an effective tool for high FE and liquid product selective electrocatalysis. Utilizing Cu or LSCO alone proves inefficient for CO_2ER indicating the role of MSI. This strategy can be a stepping stone for developing electrocatalysts for direct multicarbon products at low overpotentials.

1. Introduction

The imperative to mitigate CO_2 emissions and foster sustainability has underscored the urgent need to develop efficient methods for converting CO_2 back into high-value added fuels.[1–4] Many efforts have been made thus far to develop CO_2 conversion technologies, including thermochemistry,[5,6] electrochemistry,[7,8] and photo-electrochemistry.[9] Electrochemical reduction of CO_2 (CO_2ER), particularly using renewable energy sources like solar and wind, presents a promising avenue for creating an artificial carbon cycle.[10,11] However, this process faces significant challenges, including the stable nature of CO_2 molecules, which requires significant overpotential to initiate the reaction, and the competitive hydrogen evolution reaction (HER) in aqueous systems.[12] These challenges can lead to low conversion efficiency and poor selectivity, hindering the practical use of electrochemical CO_2 reduction.[13] The complexity of the CO_2 reduction reaction leads to a myriad of possible products, ranging from CO and CH_4 to longer carbon chain compounds like C_2H_4 and beyond.[5,14,15] Understanding whether intermediates such as CO or more reduced species are key to forming larger hydrocarbons remains crucial.[16,17] Alcohol, acetone and syngas are typical products of CO_2ER, offering potential pathways for renewable fuel switching and carbon emission reduction.[18–20] Conventional electrocatalysts have been hindered by low efficiency, poor stability, and high energy input requirements.[18,21–23] Recent advancements have aimed to address these shortcomings by improving selectivity[24,25] and controlling the co-evolution of H_2 during CO_2ER. However, proton-assisted reactions can still yield a

[a]Department of Chemistry, Indian Institute of Technology Gandhinagar, Gandhinagar, Gujarat, 382355, India. E-mail: ssharma@iitgn.ac.in
[b]Department of Materials Science and Engineering, Indian Institute of Technology Kanpur, Uttar Pradesh, 208016, India
[c]Beamline Development & Application Section, Bhabha Atomic Research Centre, Trombay, Mumbai, 400085, India

diverse array of carbon-based species, influenced by factors such as composition, applied potentials, and electrolyte properties.[26–28] While noble metals have demonstrated remarkable catalytic activity, their high cost impedes widespread commercial adoption. Consequently, attention has shifted towards exploring alternative active metals,[29,30] including zinc, copper, cobalt, and nickel.[31–33] Copper shows promise as a cost-effective electrocatalyst for CO_2ER,[5,34] but its performance and stability need enhancement. Traditionally, Cu species face stability challenges at negative potentials during CO_2ER. Supported catalysts featuring metal–support interactions (MSIs) have been employed in solid–gas reactions, providing significant advantages, including enhanced CO oxidation,[5,35,36] lower temperatures for the CO_2 catalytic reaction,[37,38] CO_2 methanation[39] and hydrogenation.[40] Recently, MSI has been applied to boost CO_2ER activity.[18] MSI play a key role in shaping the performance of heterogeneous catalysts by improving metal dispersion, optimizing the metal's electronic structure, and refining the metal–support interface.[41–45] Sharma and colleagues[5] employed a combination of electrochemical techniques and X-ray photoelectron spectroscopy (XPS) in their research to investigate the interaction between Pd^{2+} and CeO_2 in $Ce_{1-x}Pd_xO_{2-\delta}$ (with $x = 0.02$). Their findings indicate that $Ce_{0.98}Pd_{0.02}O_{2-\delta}$ serves as a reliable electrode for the electro-oxidation of H_2O to O_2, unlike CeO_2, owing to the interaction between the metal and the support material.

Perovskite materials, characterized by the ABO_3 formula, exhibit exceptional stability and electronic conductivity, making them promising for use as supports.[46,47] Specifically, lanthanum strontium cobaltite ($La_{0.8}Sr_{0.2}CoO_3$/LSCO), a perovskite-type oxide, is a compelling support for copper catalysts due to its excellent conductivity and basic nature.[48,49] The of metallic conductivity in Sr doped $LaCoO_3$ makes it a suitable host for supporting metals such as Cu.[50]

In this manuscript, we explore the development of noble metal-free metal-dispersed LSCO perovskite electrocatalysts for CO_2ER in aqueous systems. LSCO being a conducting and stable support under reducing conditions makes it an effective catalytic support for Cu nanoparticles. Variations in the Cu concentration and cell geometry were investigated to improve CO_2 conversion efficiency and product selective approach. To be specific, CO_2 reduction activity of Cu/LSCO has been extensively studied in both divided and undivided cells and both the strategies led to different product distributions and faradaic efficiencies.[51] It is possible that this study may present a general strategy which one can specifically adopt for liquid product-oriented processes through CO_2ER.

2. Materials and methods

2.1 Synthesis of the Cu/LSCO catalyst

2.1.1 Synthesis of the catalyst support (LSCO).
The preparation of copper supported LSCO catalysts involved two processes. Firstly, the conventional solution-combustion method (self-propagating high-temperature synthesis) was employed to synthesize $La_{0.8}Sr_{0.2}CoO_3$ catalysts. Stoichiometric amounts of commercial (Aldrich, 99.9%) $La(NO_3)_3 \cdot 6H_2O$, $Sr(NO_3)_2$, and $Co(NO_3)_2 \cdot 6H_2O$ precursors were dissolved in Millipore water to create a saturated aqueous solution of metal nitrates, serving as oxidizing agents. These precursors were then added to the ODH solution and heated at 80 °C with stirring to form a uniform, translucent mixture. Ignition at 450 °C of this mixture initiated an exothermic reaction, sustaining high temperatures to decompose ODH and metal nitrate salts, resulting in a dry powder. The powder was ground thoroughly and calcined for 10 hours in a Nabertherm furnace at 800 °C.

2.1.2 Deposition of copper over the LSCO support.
Copper nanoparticles (Cu NPs) were deposited on pristine LSCO substrates using the formaldehyde reduction methodology. Initially, 500 mg of pristine LSCO was dispersed in 20 mL DI of water and sonicated for 30 minutes to achieve a homogeneous solution. Subsequently, $Cu(NO_3)_2 \cdot 6H_2O$ salt solutions were prepared in ultra-pure water and added dropwise with continuous stirring. 15 mL of formaldehyde was added dropwise, maintaining the pH at 13.5 using 2.5 wt% KOH. The solution was mixed at room temperature for 30 minutes. The solution was further kept for continuous stirring for 8 hours at 60 °C. Finally, the resulting solution was centrifuged at 8000 rpm to obtain a residue, which was washed 5–6 times with ultra-pure water and dried for 24 hours. A final drying step at 80 °C yielded the catalyst in solid powder form. This process facilitated the dispersion of active nanoparticles and exposure of active sites, thereby enhancing performance through synergistic effects.

In subsequent sections, this electrode will be denoted as Cu x/LSCO (x = 10%, 20%, 30%), where LSCO represents $La_{0.8}Sr_{0.2}CoO_3$ and Cu x refers to different concentrations of copper.

2.2 Material characterisation

X-ray diffraction (XRD) analysis was conducted using a BRUKER D8 DISCOVER diffractometer equipped with a Cu Kα radiation source ($\lambda = 1.5406$ Å) to characterize the crystallinity, phase composition, and crystal structure of the synthesized catalyst. The XRD instrument was operated at a current of 40 mA and a voltage of 40 kV. Scans were performed continuously at a rate of 4° min^{-1} with a step size of 0.04°, spanning the range from 20° to 90° (2θ mode). The obtained XRD patterns were analysed using PDF-4 software from the International Centre for Diffraction Data. The synthesized catalyst's morphology was examined using a JEOL (JSM-7900F) scanning electron microscope (SEM). Additionally, an energy-dispersive X-ray spectrometer (EDS) attached to the SEM, paired with AZtec (Oxford Instruments) software, was employed to determine the composition of the catalyst. To understand the crystalline property of the synthesised catalyst, transmission electron microscopy (TEM, Techni: 20UT, FEI, USA (operated at 120 kV)) and high-resolution transmission electron microscopy (HR-TEM, Titan G2 60, FEI, USA (operated at 300 kV)) were performed. Elemental analysis was conducted using inductively coupled plasma optical emission

spectroscopy (ICP-OES, PerkinElmer Avio 200). Samples were digested in aqua regia and subsequently diluted with 2% nitric acid before analysis. CO_2 temperature-programmed desorption (CO_2 TPD) measurements were conducted to evaluate the CO_2 adsorption characteristics of the synthesized catalysts. The experiments were performed using a TPD setup equipped with a residual gas analyzer (BGA). Catalytic activity measurements were carried out in a small fixed-bed quartz reactor (6 mm outer diameter, 30 cm length), packed with 50 mg of catalyst in granular form (180–300 μm). The catalyst bed was held in place using quartz wool.

Prior to desorption measurements, the catalyst sample was pretreated by heating under a constant flow of high-purity nitrogen (30 mL min^{-1}) from room temperature to 800 °C to remove surface-adsorbed impurities. Subsequently, the sample was cooled to room temperature under a continuous CO_2 flow (30 mL min^{-1}) to allow adsorption of CO_2. After saturation, the system was purged again with nitrogen (30 mL min^{-1}), and the desorption step was initiated by linearly increasing the temperature from room temperature to 800 °C at a heating rate of 10 °C min^{-1}. The desorbed CO_2 species were continuously monitored and recorded using a BGA detector throughout the heating process. A K-type thermocouple was used to precisely monitor the catalyst bed temperature, and gas flow rates were regulated using an ALICAT MC series mass flow controller. X-ray photoelectron spectroscopy (XPS) analysis was conducted using a Thermo Fisher photoelectron spectrometer system. Measurements were performed with a K-Alpha photoelectron spectrometer, utilizing a monochromatic Al Kα X-ray source (1486.6 eV). The instrument analyzes signals originating from the surface region, typically within a depth range of 10 to 100 Å. All binding energies were calibrated to the C1s signal at 284.8 eV. The K-edges of Cu (8979 eV) and the X-ray absorption spectra were recorded at the scanning EXAFS beamline (BL-09) of the INDUS-2 synchrotron source at the Raja Ramanna Centre for Advanced Technology (RRCAT), Indore. The beamline is equipped with a Si (111) based double crystal monochromator for energy selection and a meridional cylindrical mirror (Rh/Pt coated) for collimation. The data were collected when the synchrotron source 2.5 GeV ring was operated at an injection current of 135 mA. The XAFS (XANES and EXAFS) measurements were carried out at room temperature Cu K-edge in fluorescence mode and Co K-edge in transmission mode. The ion chambers were filled with N_2, He, and Ar for Cu and for the electrocatalysts. The second crystal of the monochromator was 60% detuned during the data collection to suppress the higher harmonic components. The energy calibration was performed using Cu metal foil as a reference. The standard normalization and background subtraction procedures were executed using the ATHENA software version 0.9.26 to obtain normalized XANES spectra.[52] Fourier transformed (FT) values of the EXAFS oscillations were calculated to observe the $|\chi(R)|$ vs. R space spectra. The fitting was done using ARTEMIS software version 0.9.26 which uses FEFF6 and ATOMS programs to simulate the theoretical scattering paths according to the crystallographic structure.[53] The data fitting

for Cu K-edge was in the k range of 2.9–7.9 Å^{-1} and R range of 1.1–3.6 Å.

ICP-OES analysis determined the actual Cu contents to be 7.2 wt%, 16.8 wt%, and 21.5 wt% for Cu 10/LSCO, Cu 20/LSCO, and Cu 30/LSCO, respectively. The deviations from nominal values are attributed to factors such as incomplete precursor deposition, material loss during processing, or limited copper uptake by the LSCO support. Nevertheless, designations are based on the nominal copper content targeted during synthesis and are used throughout the manuscript for consistency and ease of comparison.

2.3 Cell design and electrochemical measurements

A potentiostat (CHI 660E instrument) workstation was utilized to assess the electrochemical measurements. The electrochemical CO_2 reduction experiments employed an undivided cell (custom-built electrochemical four-neck cell) and divided (H-type cell) setup. In the divided cell configuration, a Nafion 117 proton exchange membrane divided the cathode and anode chambers. The cathode chamber was isolated from the anode by a cation-exchange membrane (Nafion), and it was equipped with silicon O-rings. Fresh catalyst loading over a glassy carbon electrode (GCE) was ensured for experiments to mitigate the influence of catalyst layer degradation on product distribution and to facilitate accurate gas analysis. Both electrochemical cells were sealed tightly to ensure all generated gases were captured during the experiments. In each electrolysis experiment, the cell comprised a Cu x/LSCO/GCE working electrode (having a fixed area of 0.071 cm^2) and a platinum counter electrode. The potential was measured relative to an Ag/AgCl reference electrode. The electrolyte (0.5 M $NaHCO_3$), comprising doubly distilled deionized water and reagent-grade chemicals, was prepared. Prior to cyclic voltammetry (CV) testing, the electrolyte containing bicarbonate was purged with nitrogen followed by carbon dioxide at a flow rate of 15 sccm (high-purity grade, >99%). Nitrogen purging served to eliminate dissolved oxygen and establish an inert atmosphere. The glassy carbon electrode underwent polishing with a polishing suspension and rinsing with copious amounts of deionized water and isopropanol to remove any residual polishing suspension. Impedance analysis was conducted over a frequency range of 100 kHz to 0.001 Hz at room temperature using a 0.5 M $NaHCO_3$ electrolyte solution.

2.4 Quantification of reaction products and CO_2 temperature programmed desorption study

After performing the CO_2ER experiment, the products were syringed out by a high-precision airtight syringe. These products were then identified and quantified using gas chromatography (GC). The detection was carried out at Dhruva CIC Baroda for gas detection and with a Nucon gas chromatograph for liquid detection.

For both gas and liquid analyses, nitrogen and argon were used as carrier gases, respectively. A thermal conductivity detector (TCD) and flame ionization detector (FID) coupled with a methaniser were employed to quantify the generated

gaseous and liquid products during the electroreduction process. The CHROMOSORB 101 capillary column was used for liquid product analysis.

CO$_2$ temperature-programmed desorption (CO$_2$-TPD) measurements were conducted to evaluate the CO$_2$ adsorption characteristics of the synthesized catalysts. The experiments were performed using a TPD setup equipped with a residual gas analyzer (BGA). Catalytic activity measurements were carried out in a small fixed-bed quartz reactor (6 mm outer diameter, 30 cm length), packed with 50 mg of catalyst in granular form (180–300 μm). The catalyst bed was held in place using quartz wool.

Prior to desorption measurements, the catalyst sample was pretreated by heating under a constant flow of high-purity nitrogen (30 mL min^{-1}) from room temperature to 800 °C to remove surface-adsorbed impurities. Subsequently, the catalyst sample was cooled to room temperature under a continuous CO$_2$ flow (30 mL min^{-1}) to allow adsorption of CO$_2$. After saturation, the system was purged again with nitrogen (30 mL min^{-1}), and the desorption step was initiated by increasing the temperature from room temperature to 800 °C at a heating rate of 10 °C min^{-1}. The desorbed CO$_2$ species were continuously monitored and recorded using the BGA detector throughout the heating process. A K-type thermocouple was used to precisely monitor the catalyst bed temperature, and gas flow rates were regulated using an ALICAT MC series mass flow controller.

2.5 Computational method

Electronic structure calculations were performed using density functional theory (DFT) implemented in the CP2K program suite. We employed the Quickstep module in the CP2K program to perform the above-mentioned calculations. Exchange–correlation potentials were treated within the generalized gradient approximation (GGA) employing the Perdew–Burke–Ernzerhof (PBE) functional. The GGA formalism has been utilized in producing very accurate results when investigating the adsorption of CO$_2$ and electrochemical reduction of CO$_2$ on Cu$_4$ decorated LSCO surfaces. The PBE functional combined with the double-ζ valence plus polarization (DZVP) basis set was used to optimize the LSCO surfaces and intermediates using the Mol-Opt method with the energy cut-off set to 415 Ry in the CP2K program suite. Valence electrons were explicitly modelled, while core electrons were treated using norm-conserving Goedecker–Teter–Hutter (GTH) potentials. In particular, GTH potentials with 1, 4, 6, 17, 11, 11 and 10 valence electrons were assigned for H, C, O, Co, Cu, La and Sr, respectively. The Brillouin zone integration was carried out using a reciprocal space mesh centered on the gamma point. We implemented DFT-D3 van der Waals corrections using Grimme in order to consider long-range dispersion forces into account to measure the interaction between the adsorbate and CuO surfaces accurately. All these calculations were performed under periodic boundary conditions.

Herein, CO$_2$ electro-reduction has been investigated at LSCO (110) surfaces decorated with Cu$_4$ clusters using the DFT method. We have chosen 5 × 3-unit cells consisting of 48 La, 12 Sr, 60 Co and 150 O atoms, respectively. The slab size consisted of three layers: the two layers at the bottom were fixed, and the top layer was allowed to relax for optimizing the intermediate species. Also, we set a slab height of 15 Å along the [110] direction in order to avoid the interactions with the periodic images of the slab. The intermediate species were optimized over XCu$_4$ (X = 3–5) decorated LSCO (110) surfaces using the PBE/DZVP level of theory. The atoms of both the adsorbate and the topmost layer of the slab were allowed to relax without constraints until the residual forces on all atoms reached 1.0 × 10^{-2} atomic units.

3. Results and discussion

3.1 Structural and morphological characterization

The X-ray diffraction (XRD) patterns (Fig. 1) of all x% (0–30%) LSCO samples show no impurity phases compared with the standard LSCO (ICDD PDF# 01-075-8569). As shown in Fig. 1, all the diffraction peaks of the compounds can be identified well as a rhombohedral crystal structure. The prominent peaks at 2θ = 23.1°, 32.8°, 33.14, 47.4°, 58.8° are attributed to the crystal planes of (012), (110), (104), (024) and (214) with the $R\bar{3}c$ space group symmetry for the LSCO catalyst. Scherrer's equation (expressions are given in the ESI in section 2.1†) was used to calculate the crystallite size, and the estimated values are 16.9 nm, 17.1 nm, 15.9 nm and 14.6 nm for LSCO, Cu 10/ LSCO, Cu 20/LSCO and Cu 30/LSCO respectively. The XRD patterns confirm that all synthesized formulations exhibit crystallinity. The lack of segregated Sr and Co phase species suggests the formation of a single-phase compound. Additionally, strong peaks attributed to metallic copper were observed at
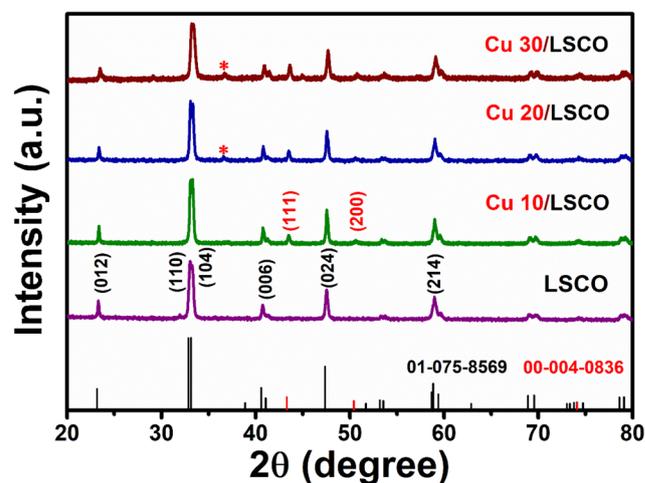

Fig. 1 Comparative X-ray diffraction patterns of crystalline LSCO, Cu 10/LSCO, Cu 20/LSCO and Cu 30/LSCO. The asterisks (*) denote the presence of the (111) plane of the Cu$_2$O phase, distinct from the metallic Cu peaks. This comparison highlights the structural evolution and phase composition as a function of increasing copper content in the LSCO matrix.

$2\theta = 43.29°$ and $50.43°$. These intense Bragg reflections correspond to the (111) and (200) reflections of face-centered cubic (FCC) copper symmetry (ICDD PDF# 00-004-0836). In the case of Cu 20/LSCO and Cu 30/LSCO, we observed an additional peak corresponding to bulk Cu_2O.

The SEM morphological studies shown in Fig. S6† reveal that the nanoparticles are irregular spherical in shape. The surface feature of the catalyst is difficult to distinguish. As the concentration of copper increases from 10% to 30%, larger particles emerge due to the formation of van der Waals clusters of smaller particles. This change in concentration also leads to a shift in the morphology of the particles, transitioning from irregular spherical shapes to more sheet-like structures.

X-ray photoelectron spectroscopy (XPS) measurements were conducted to examine the chemical state of Cu in the Cu/LSCO catalysts with varying Cu loadings (Cu 10, Cu 20, and Cu 30). The Cu 2p spectra (Fig. 2) exhibit clear differences that reflect changes in the surface chemistry of Cu as the loading increases.

For both Cu 10/LSCO and Cu 20/LSCO, the Cu $2p_{3/2}$ peak appears sharply at ~932.5 eV, which is characteristic of metallic Cu (Cu^0). A weak satellite feature between 940 and 945 eV is also present, indicating the presence of Cu^+ species, typically associated with Cu_2O (Fig. 2a and b). The similarity in spectral features between Cu 10/LSCO and Cu 20/LSCO suggests that both samples have nearly identical surface compositions, consisting primarily of metallic Cu with minor contributions from Cu^+. This composition is consistent with minimal surface oxidation and a high density of accessible active sites. In contrast, the Cu 30/LSCO sample shows a broader main peak along with intense satellite features, characteristic of Cu^{2+} species. The stronger presence of Cu^{2+} indicates a greater degree of surface oxidation at higher Cu loadings. Additionally, the spectral broadening in Cu 30/LSCO may also suggest the onset of Cu agglomeration, which can lead to reduced dispersion and a lower number of catalytically active surface sites. The higher catalytic activity observed for Cu 10/LSCO and Cu 20/LSCO

compared to Cu 30/LSCO can thus be attributed to their favorable surface composition—dominated by Cu^0 and Cu^+—and greater dispersion of active Cu species as shown in XPS studies (Fig. 2c). Notably, the presence of Cu^+ (Cu_2O) is particularly important, as it has been reported in the literature to play a key role in promoting C–C coupling reactions, a key step in acetone formation.[54,55] The combination of these surface features in Cu 10/LSCO and Cu 20/LSCO provides an optimal environment for such transformations, whereas the more oxidized and potentially agglomerated Cu 30/LSCO exhibits diminished activity. Detailed XPS data for LSCO have been reported in the work of Dhakar *et al.*[56]

To investigate the local coordination environments and oxidation state of Cu and Co in the Cu decorated LSCO catalyst, we performed Cu K-edge and Co K-edge X-ray absorption spectroscopy (XAS), including both extended X-ray absorption fine structure (EXAFS) and X-ray absorption near edge structure (XANES) analyses. The effect of varying Cu loading (10, 20, and 30 wt%) on the structural and electronic states was systematically examined. Cu K-edge XANES analysis (Fig. S8†) depicts the normalized Cu K-edge XANES spectra of Cu-loaded LSCO compared with Cu foil (Cu^0), Cu_2O (Cu^+), and CuO (Cu^{2+}) standards. The XANES spectra for Cu 10/LSCO and Cu 20/LSCO samples closely resemble that of Cu foil, particularly in terms of edge energy indicating that Cu exists predominantly in the metallic state (Cu^0) at these loadings. It suggests the presence of bulk Cu^0 species. Subtle shifts in the edge position and from Cu 10/LSCO to Cu 20/LSCO suggest minor changes in the local electronic environment or coordination geometry, potentially arising from different degrees of dispersion or site occupancy. In contrast, the Cu 30/LSCO sample shows a shift toward higher edge energy, consistent with the oxidized Cu^{2+} state seen in CuO. These findings indicate a clear evolution of Cu speciation with loading: from metallic Cu at lower concentrations to oxidized Cu^{2+} at higher loadings.

The corresponding Fourier-transformed EXAFS spectra (Fig. 3a) further reveal the local coordination structure around Cu. For Cu 20/LSCO, a dominant peak appears at ~2.3 Å
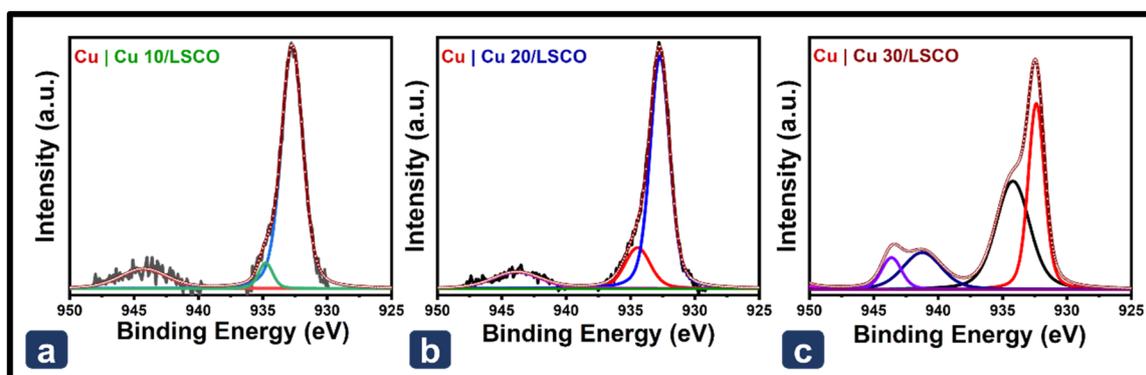

Fig. 2 High-resolution deconvoluted Cu $2p_{3/2}$ XPS spectra of (a) Cu 10/LSCO, (b) Cu 20/LSCO, and (c) Cu 30/LSCO samples. Cu 10/LSCO and Cu 20/LSCO show peaks consistent with Cu^0 and Cu^+ (Cu_2O), while Cu 30/LSCO exhibits broader features and strong satellite peaks characteristic of Cu^{2+} (CuO), indicating increased oxidation at higher loading.
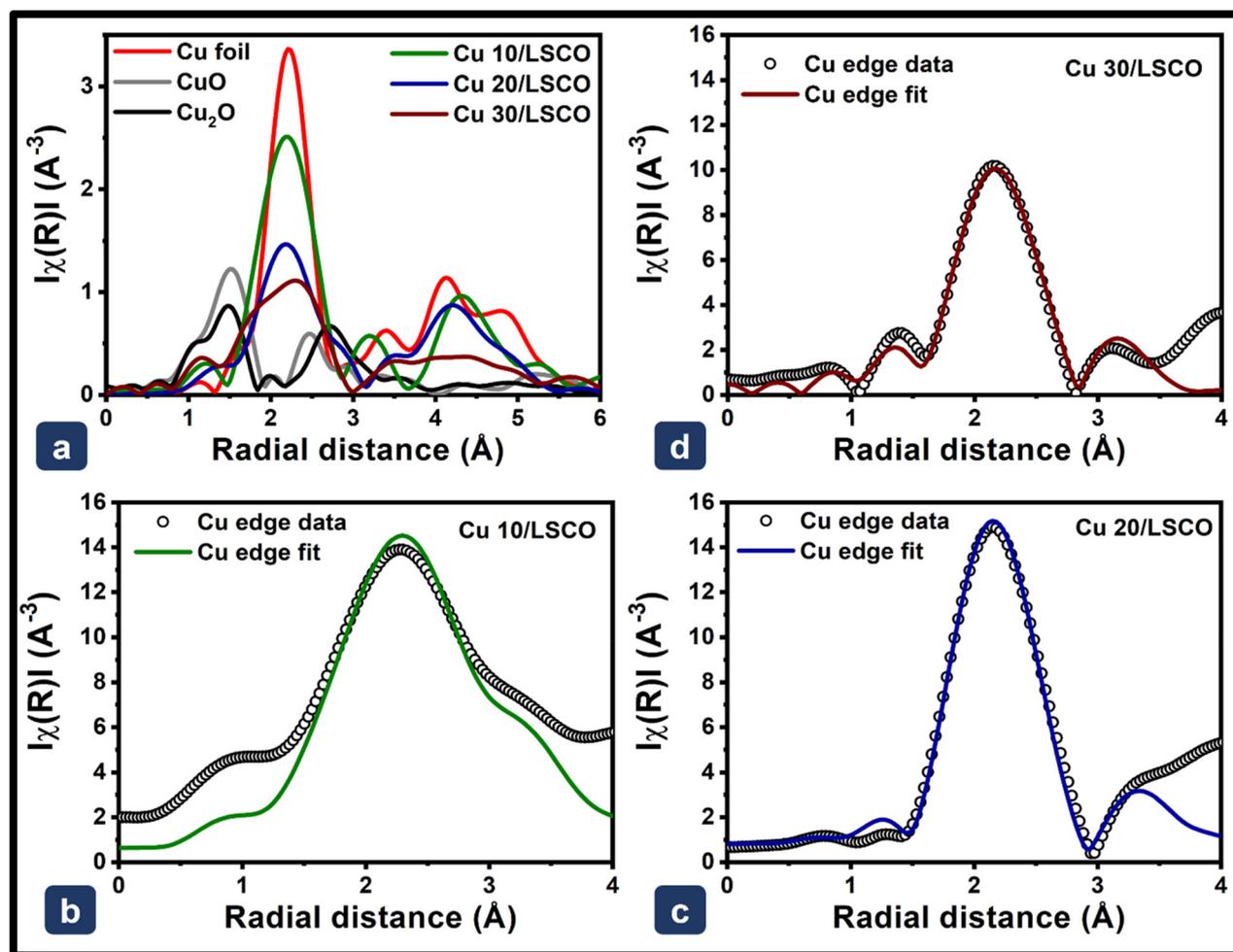
Fig. 3 (a) Fourier-transformed Cu K-edge EXAFS spectra of Cu x/LSCO samples (x = 10%, 20%, and 30%) compared with the reference spectra of Cu foil, CuO, and Cu$_2$O. (b–d) Fourier-transformed Cu K-edge EXAFS data (scatter points) and the corresponding fitting curves (solid lines) for (b) Cu 10/LSCO, (c) Cu 20/LSCO, and (d) Cu 30/LSCO.

characteristic of Cu–Cu scattering in metallic Cu. This clearly indicates the presence of bulk metallic Cu domains. The good agreement between the experimental data and EXAFS fitting using metallic Cu as a reference model further validates this assignment (Fig. 3).

Higher-shell features are damped, suggesting moderate disorder, but the core Cu–Cu bonding remains intact. This confirms that at intermediate Cu loadings (*e.g.*, 10 and 20 wt%), Cu predominantly exists as metallic clusters or nanoparticles, rather than as atomically dispersed oxidized species (Fig. 3b and c). In contrast, Cu 30/LSCO shows a shift in the main peak to ~1.9 Å, typical of Cu–O coordination, along with the absence of metallic Cu–Cu features (Fig. 3d). This indicates a transition to a more oxidized Cu environment at higher loadings.

All key parameters obtained from the XAFS analysis are summarized in Table 1, which presents the EXAFS fitting results at the Cu K-edge for Cu *X*/LSCO samples with x = 10%, 20%, and 30%.

From the BF-TEM images shown in Fig. 4a, c, and e, it can be observed that all the LSCO supported catalysts exhibit a sheet-like morphology. The Cu NPs decorated on the surfaces were shown to have a distinct black contrast on the LSCO sheets as shown in the marked regions on all the three BF-TEM images. It is particularly noteworthy to mention that the particle diameters of the Cu NPs measured on the LSCO surfaces are ranged from approximately 8 to 10 nm for Cu 10/LSCO and Cu 30/LSCO, whereas they were 4–6 nm for Cu 20/LSCO. The crystals exhibited heterogeneity in size, polydispersity, and well-defined crystallinity. With an increase in the Cu NP loading, random agglomeration of Cu nanoparticles on the LSCO surface is evidenced by the dark patched region in BF-TEM images. At a higher concentration (30%), even larger agglomerates form as a result of van der Waals clustering causing lattice mismatch between the LSCO support and Cu NPs. This is evident from the HR-image in Fig. 4b, d and f. The region of interest, shown as the marked region on the BF-TEM images, was further observed under HR-mode to properly

Table 1 EXAFS fitting parameters at the Cu K-edge for Cu x/LSCO samples with x = 10%, 20%, and 30%

Sample	Bond	N	R (Å)	σ^2 (Å^2)	ΔE_0 (eV)	R factor
Cu edge	Cu–Cu1	12.0	2.58 ± 0.02	0.0030 ± 0.0010	6.480 ± 2.545	0.016
Cu 10/LSCO	Cu–Cu2	6.0	3.52 ± 0.03	0.0030 ± 0.0010		
Cu edge	Cu–Cu1	12.0	2.54 ± 0.01	0.0070 ± 0.0013	−4.389 ± 1.442	0.007
Cu 20/LSCO	Cu–Cu2	6.0	3.55 ± 0.03	0.0086 ± 0.0029		
Cu edge	Cu–Cu1	12.0	2.55 ± 0.01	0.0129 ± 0.0028	−8.425 ± 1.668	0.018
Cu 30/LSCO	Cu–Cu2	6.0	3.57 ± 0.02	0.0135 ± 0.0042		
	Cu–O	2.0	1.87 ± 0.03	0.0178 ± 0.0097		
	Cu–Cu	12.0	2.88 ± 0.03	0.0260 ± 0.0055		

N: coordination number; R: bond distance; σ^2: Debye–Waller factor; ΔE_0: the inner potential correction. R factor: goodness of fit.

distinguish the lattice fringes of the Cu NPs and the LSCO. The HRTEM image of Cu 10/LSCO showed distinct lattice fringes with spacings of 2.12 Å and 3.89 Å, corresponding to the (111) plane of copper (Cu) and the (012) plane of LSCO, respectively (Fig. 4). For Cu 20/LSCO, the HRTEM image showed lattice fringes with spacings of 2.17 Å and 2.67 Å, matching the (111) plane of Cu and the (110) plane of LSCO. Likewise, in the case of Cu 30/LSCO, lattice fringes were observed with spacings of 2.17 Å and 2.68 Å, corresponding to the (100) plane of Cu and the (110) plane of LSCO. It can be observed from Fig. 4d and f that the lattice mismatch is not severe in the case of Cu 20/LSCO and Cu 30/LSCO supported catalysts, indicating a formation of near-coherent interfaces between Cu NPs and LSCO. Similarly, in the case of Cu 10/LSCO, even though the mismatch is present, the lattice periodicity is somewhat maintained, indicating a plausible formation of a semi-coherent interface. This may affect the overall electrocatalytic activity towards CO_2 which will be discussed in the later sections.

The fine scale microstructures of the post-reacted Cu 20/LSCO catalyst is shown in Fig. S7.† Fig. S7a† shows a low magnification bright field image of the catalyst, and the contrast due to different thicknesses can be observed in the catalyst sample. This thickness contrast may arise from the agglomeration of Cu NPs on the LSCO surface. Correspondingly, another low magnification bright field image is also displayed in Fig. S7b.† Similar to Fig. S7a,† grey contrast and dark contrast regions can be observed. The grey contrast region is referred to the LSCO whereas the dark contrast region can originate either due to the thickness contrast or the presence of agglomeration of the Cu NPs after the reaction was completed. To ascertain the fact, first the SADP from the region corresponding to Fig. S7a† was indexed, which confirms the presence of Cu and LSCO in the sample. This also confirms that Cu is present in elemental form only. Additionally, the HAADF image and the corresponding elemental maps are also displayed in Fig. S7d and S7e.† The elemental maps shows that agglomerated Cu is present on the LSCO surface, which could not be observed in the pre-reaction sample where Cu NPs could be observed on the LSCO surface.

3.2 CO_2 electrochemical measurements

Electrochemical CO_2ER studies were conducted in an undivided cell to investigate the electrocatalytic efficacy *i.e.*, the effect of CO_2 purging and copper loading on the synthesised electrocatalysts. Cyclic voltammetry (CV) and linear sweep voltammetry (LSV) scans in the potential window between −0.9 V and 0.62 V *vs.* RHE were performed. In this section, the electrochemical behaviour of the catalyst was studied under both CO_2 and N_2 purging conditions.

Initially, during CO_2 purging, there were hardly any discernible changes in the current when solely employing the LSCO catalyst compared to nitrogen purging (Fig. S1a†). However, upon introducing copper onto the LSCO catalyst, a significant increase in the current was noted under CO_2 purging conditions (Fig. S1c†). Under nitrogen purging, the current density was recorded at −9.31 mA cm^{-2}, which experienced a significant increase to −11.36 mA cm^{-2} upon switching to CO_2 purging (Fig. S1c†). This indicates a favourable electrochemical response to CO_2 by the copper loaded system. Furthermore, as the copper loading increased to 20%, the current density exhibited a substantial increase, increasing from −11.76 mA cm^{-2} in the nitrogen purged system to −20.28 mA cm^{-2} after CO_2 purging (Fig. S1e†). This highlights the synergistic effect of copper loading on enhancing the catalytic performance of the LSCO catalyst, particularly in the presence of CO_2. Subsequently, when the copper concentration was increased from 20% to 30%, in the nitrogen purging system, the current increased from −11.76 to −16.46 mA cm^{-2}. However, intriguingly, in the CO_2 environment, the current only marginally increased to −20.23 mA cm^{-2}, which was comparable to the current observed with Cu 20/LSCO in the CO_2 environment (Fig. S1g†). These results suggest that while increasing copper loading initially boosts the catalytic activity, a certain threshold due to active site saturation comes about at Cu 20/LSCO and further increases in the catalytic activity is not significant in CO_2-rich environments. These comparative studies, as depicted in Fig. 5a, provide crucial insights into the catalytic behaviour of the various formulations. Remarkably, the initial current density of −2.48 mA cm^{-2} exhibited a substantial increase to −11.36 mA cm^{-2} upon introducing Cu 10/LSCO. This notable enhancement in current density highlights the pivotal role of copper loading in augmenting the electrocatalytic activity. Furthermore, as the copper loading is escalated from 10% to 20% and 30%, the current density increases from −11.36 mA cm^{-2} to approximately −20.28 mA cm^{-2} for 20% copper loading, while reaching −20.23 mA cm^{-2} for 30%
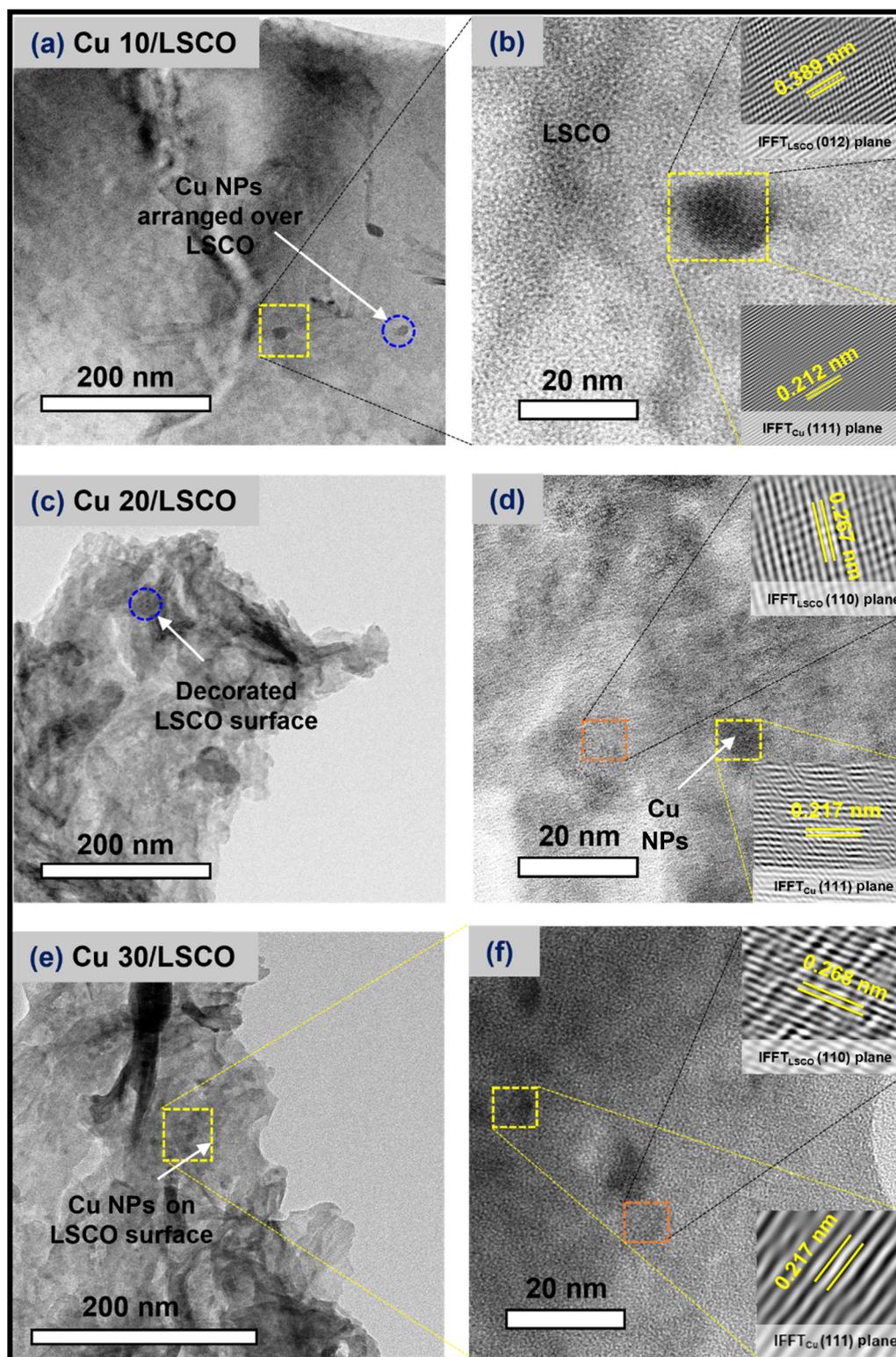
Fig. 4 The bright-field TEM (BF-TEM) images of the supported catalysts are shown in (a, c and e), accompanied by high-resolution images in (b, d and f) for Cu10/LSCO, Cu 20/LSCO, and Cu 30/LSCO respectively. These images confirm the presence of Cu nanoparticles on the LSCO surface.

loading, as illustrated in Fig. 5a. The observed severe bubbling on the electrodes upon the decoration of copper nanoparticles over the LSCO support signifies a significant enhancement in catalytic activity. These findings demonstrate the pivotal role of copper nanoparticle decoration on the LSCO support in boosting the catalytic performance for CO_2 electroreduction,
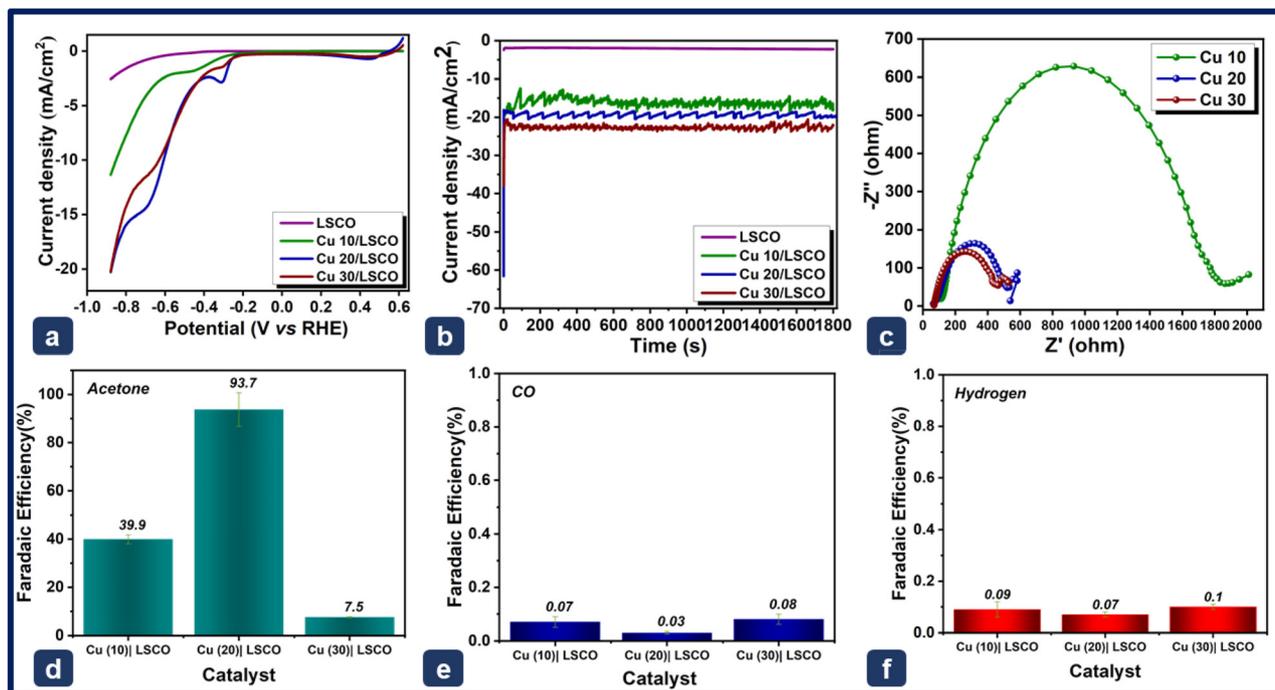
Fig. 5 Comparative (a) linear sweep voltammetry response in the potential range of 0.62 V to −0.9 V *vs*. RHE in a CO_2 purged system. (b) Chronoamperometry profiles at a fixed potential of −0.9 V for the synthesised LSCO (purple trace), Cu 10/LSCO (olive trace), Cu 20/LSCO (blue trace) and Cu 30/LSCO (wine trace) in 0.5 M $NaHCO_3$ electrolyte. (c) Comparison of electrochemical impedance spectroscopy (EIS) plots of all copper decorated perovskite catalyst formulations at −0.58 V *vs*. RHE in 0.5 M $NaHCO_3$ electrolyte. Faradaic efficiencies for (d) acetone, (e) carbon monoxide and (f) hydrogen products.

thus holding promise for advancing sustainable CO_2 conversion technologies.

The electrochemical impedance spectroscopy (EIS) analysis[57,58] was conducted on Cu 10/LSCO, Cu 20/LSCO, and Cu 30/LSCO electrodes to probe the electron transfer and kinetics involved in CO_2ER. In line with the associated linear sweep voltammetry (LSV) results, the charge transfer resistance (R_{ct}), which represents the resistance against the electron transfer, significantly decreased with an increase in the copper loading in Cu 10, Cu 20, and Cu 30, going from 1751.5 ohm to 455.9 ohm and 388.06 ohm, respectively (Fig. 5c). The semicircular diameter of the Nyquist plot for Cu 20/LSCO (R_{ct} = 455.9 Ω) is much smaller than that of Cu 10/LSCO (R_{ct} = 1751.5 Ω), suggesting a remarkably improved charge transfer on increasing the copper concentration. The current and impedance are indicators of the electrical behaviour of the catalyst, such as its conductivity or resistance to electron flow. However, the specific reactions and products formed are determined by the catalytic activity, which can be influenced by factors like the surface structure, active sites, and chemical composition of the catalyst. Although the catalyst compositions (Cu 20/LSCO and Cu 30/LSCO) have similar electrical properties, resulting in comparable current and impedance values, the differences in the amount of copper and other components can lead to variations in catalytic activity, affecting the selectivity and yield of the products. This can occur due to changes in surface

chemistry, availability of active sites, or interactions with reactant molecules.

Therefore, while electrical properties can provide valuable insights into catalyst behaviour, they do not necessarily dictate the specific reaction pathways or product distributions.

The chronoamperometry (CA) test was performed to measure the activity and steady state stability of the synthesised electrocatalyst. Here current density was measured for 1000 s while a constant potential of ∼−0.9 V was applied in 0.5 M $NaHCO_3$ electrolyte solution (Fig. 5b). Choosing ∼−0.9 V for the chronoamperometry could reflect an optimal overpotential where the catalyst, like our support LSCO, remains stable. The experiment was conducted for all catalytic formulations. The steady state takes around 100 seconds to achieve a stable profile. Currents reached after 1000 s were reported as −2.07 mA cm^{-2}, −17.10 mA cm^{-2}, −19.43 mA cm^{-2} and −27.67 mA cm^{-2} for LSCO, Cu 10/LSCO, Cu 20/LSCO and Cu 30/LSCO respectively.

3.3 CO_2 electroreduction and faradaic yields

In order to corroborate that the reduction current is indeed due to carbon dioxide reduction, quantitative analysis of the product gases resulting from the CA experiment (−0.9 V for 1000 s) was carried out in a gas chromatograph. After the CA experiment, the gas samples in the head space of the sealed electrochemical cell were collected and injected to gas

chromatography. Liquid products were also collected from the seal proof electrochemical cell after the CA experiment. The gas chromatography analysis revealed the presence of H_2, CO, and acetone as the gaseous and liquid products, respectively. Although methane and ethylene were observed in certain experiments, their quantities varied, and it was difficult to quantify them.

Faradaic efficiency refers to the ratio of the desired product formed at the electrode surface to the total charge passed during the reaction. Liquid product analysis revealed the presence of acetone, with varying yields depending on the Cu loading. Specifically, the Cu 10/LSCO catalyst resulted in an acetone yield of 39.9%, while the Cu 20/LSCO catalyst demonstrated a much higher yield of 93.7%. In contrast, the Cu 30/LSCO catalyst produced a significantly lower acetone yield of only 7.5% (Fig. 5d). Gas analysis indicated the presence of CO (Fig. 5e) and hydrogen (H_2) (Fig. 5f) as the byproducts, with different concentrations observed for each Cu loading.

We achieved a maximum faradaic efficiency (FE) of 93.7% for acetone production at −0.9 V (vs. RHE) using Cu 20/LSCO, where the FE for H_2 was at its minimum (0.07% at −0.9 V). In contrast, neither the Cu NPs nor LSCO generated acetone, with H_2 being the main product. Notably, Cu 20/LSCO demonstrated excellent electrocatalytic activity for the formation of acetone, distinguishing it from individual Cu nanoparticles or LSCO, which primarily produced H_2 in CO_2ER. This demonstrates the significance of the metal–support interaction in facilitating the production of acetone from CO_2 via electrochemical reduction reactions.

Reproducibility of the results was confirmed through three replications of the experiments, showing nearly identical patterns in the outcomes across different batches of synthesized electrocatalysts. In our investigation of the electroreduction of CO_2, we have observed that CO may serve as a precursor to acetone formation. While other intermediates may also exist, they are currently beyond the detection limit of our instrument.

Furthermore, to assess the stability of the best performing electrocatalyst (Cu 20/LSCO) over time, we conducted long-term CO_2ER experiments under a constant applied voltage of −0.9 V. While we observed a small decline in the absolute value of the current over a period of 40 thousand seconds, the catalyst demonstrated overall stability, which is a crucial factor for potential commercialization. While the catalyst demonstrated stability in current, it was crucial to analyze the product distribution over time. Therefore, we quantified the products at different intervals also and observed that the faradaic efficiency (FE) decreased over time. For the Cu 10/LSCO catalyst, when the CO_2ER experiment was conducted for 1000 seconds, the faradaic efficiency for acetone production was ~40%, with CO and hydrogen production at 0.08% and 0.09%, respectively. Extending the duration to 1800 seconds, CA resulted in a significant decrease in the faradaic efficiency of acetone to 13.7%, while CO efficiency decreased from 0.08% to ~0.01%. Interestingly, hydrogen production more than doubled, with its faradaic efficiency increasing from 0.09% to

0.3%. This suggests that the Cu 10/LSCO catalyst is particularly efficient at producing acetone, a C3 product, only within the initial 1000 seconds of the reaction.

We performed similar experiments for extended periods with the Cu 20/LSCO and Cu 30/LSCO catalysts. For the Cu 20/LSCO catalyst, the faradaic efficiency of acetone further decreased from 93.7% to 13.3% on enhancing the CA time from 1000 to 1800 seconds. However, CO production decreased from 0.03% to 0.02%, while hydrogen production increased from 0.073% to 0.08% (Fig. S4†). In the case of the Cu 30/LSCO catalyst, the faradaic efficiency of acetone further decreased from 7.5% to 5.1% in enhancing the CA time from 1000 to 1800 seconds. Conversely, CO production increased from 0.08% to 0.09%, and hydrogen production remained almost same 0.1% (Fig. S4†). These results indicate that while the initial efficiency of acetone production is high for shorter durations, prolonged reaction times lead to a notable decrease in acetone efficiency and shifts in the production of other products such as CO and hydrogen.

The overall electrochemical behaviour of all the catalysts highlights the role of catalyst composition and reaction time in determining both the distribution and efficiency of the final products. Specifically, as the copper concentration in the catalyst increased from 10% to 30%, larger agglomerates formed due to van der Waals clustering among smaller copper nanoparticles. This clustering likely leads to lattice mismatch between the copper nanoparticles and the support material. At higher copper loadings, agglomeration of copper nanoparticles becomes more pronounced, which can negatively impact the catalyst's stability and long-term performance. Therefore, achieving an optimal copper loading is crucial for maintaining sustained catalytic activity. The enhanced performance observed at intermediate copper concentrations may be attributed to a balance between active site saturation and the prevention of nanoparticle agglomeration, maximizing the exposure of active sites for efficient CO_2 reduction. Smaller particle sizes in this optimal range increase the electrochemically active surface area, further boosting catalytic efficiency.

Other than the several aspects mentioned above, the unique crystalline metal–support interaction and composite structure of Cu/LSCO exhibits novel electrocatalytic properties in CO_2 giving acetone with high FE. Cu NPs on the LSCO support introduce abundant active sites for CO_2ER.[59] The unique electronic structure of Cu facilitates CO_2 adsorption and activation, while the crystalline LSCO support modulates the electronic structure of Cu active sites and enhances the electron transfer properties, optimizing their interaction with CO_2 intermediates.[5,60–62] Overall, the crystallinity, metal–support interaction and facile electron transfer in the composite structure of Cu/LSCO catalysts imparts a unique electrocatalytic activity for CO_2 electro reduction process.

It is clear that the current cell geometry (undivided cell) affords the significant liquid product, acetone. Acetone production is a complicated 16 electron process and kinetically should be a slow process.[18] Nevertheless, Cu 20/LSCO gives ~93% efficiency for this product. In order to be completely

certain about the experimental results, the experiments were repeated multiple times, and each time the efficiency of acetone production was nearly the same. So, one may ask how a kinetically sluggish process of acetone formation is even possible with such a high FE (above 90%) and in such a short time (within 1000 seconds). Is it the efficacy of the catalyst alone or the cell geometry also has a role? Cell geometry is an important parameter because in an undivided cell setup, the anode of CO_2ER is near the cathode and will have easy access to protons and the right pH environment for multielectron processes such as alcohol or acetone production.[63] In contrast, in a divided cell the anode of CO_2ER will have to wait for protons to diffuse near to its surface. During this time delay, intermediates such as CO might form and leave the catalyst's surface without going to higher order multielectron processes. To test this concept, we conducted CO_2 electroreduction experiments in an undivided cell to verify if acetone formation is independent of the cell geometry.

We replicated the experiment employing a divided cell setup, incorporating a Nafion membrane to segregate the cathodic and anodic chambers. Our aim with this modified setup was to understand the mechanisms of acetone synthesis.[64] We noticed a significant decrease in the catalytic current ($\sim$12 mA cm^{-2}) in the H cell and the products obtained were CO, CH_4 and H_2 with 4.3%, 1.6% and 3.7% FE respectively. Surprisingly, we could not detect acetone. This finding suggests that the effectiveness of the catalytic process diminishes with greater spatial separation between the electrodes, impacting the overall efficiency of the electrochemical reaction. Then, we made an adjustment by substituting the glassy carbon working electrode with a gas diffusion electrode (GDE) to enhance the reaction kinetics (Fig. S2†). A porous composite electrode, known as a GDE, typically consists of polymer-bonded catalyst particles and a carbon support. Their high porosity and partial hydrophobicity facilitate the formation of a unique gas–solid–liquid three-phase interface, ensuring uniform dispersion of reactants across the catalytic surface. This strategic alteration yielded the measurable acetone formation ($\sim$3–4% FE) with CO, CH_4 and H_2 with 0.6%, 0.05% and 1.3% FE respectively. Clearly, at elevated kinetics (large area of working electrode), the Cu 20/LSCO catalyst is capable of producing acetone. Nevertheless, the low FE of acetone suggests that unlike an undivided cell, a divided cell geometry is not appropriate for acetone production. Obviously, the counter electrode environment near the vicinity of the working electrode is essential for the liquid product because the access to protons is easier, the pH environment is accurate and possibly these are the vital parameter for acetone formation in the present case. Now, if this can be a general strategy for other supported systems as well is a question which needs more experiments with several catalytic systems.

The CO_2-TPD profile (Fig. S5†) of Cu 20/LSCO reveals a broad distribution of basic sites—spanning weak to strong strength categories—suggesting high surface heterogeneity and reactivity, ideal for stabilizing intermediates and facilitating CO_2 adsorption. Given the similar oxidation states and dis-

persion observed in Cu 10/LSCO, this profile is representative of both Cu 10/LSCO and Cu 20/LSCO. In contrast, Cu 30/LSCO displays significant surface oxidation to Cu^{2+} (CuO) and sharper low-temperature CO_2 desorption peaks, indicative of fewer and weaker basic sites. This suggests a loss of strong CO_2 adsorption sites and a likely reduction in C–C coupling capability. Furthermore, the presence of Cu agglomeration at higher loading, inferred from both the XPS peak broadening (Fig. 2c) and the narrow TPD profile, may also reduce the number of accessible active sites. As such, the lower dispersion and higher oxidation state in Cu 30/LSCO are directly correlated with its diminished catalytic performance in acetone production.

3.4 Plausible mechanism

The exact mechanism behind acetone formation during CO_2ER is not entirely clear, and we avoid proposing a specific mechanism that may be inaccurate. The distribution of products from CO_2ER is influenced by the electrode materials and reaction conditions.[65,66] Increasing the copper content in perovskite catalysts boosts the catalytic activity for CO_2 electroreduction by providing more active sites for CO_2 adsorption and activation, thus accelerating reaction rates.[67,68] In CO_2ER, the reactants primarily consist of dissolved CO_2 and protons transported from the anode through the solution. It is beyond any doubt that CO might serve as a precursor to acetone formation, and other intermediates may also play a role in the reduction process. It is likely that the two important intermediates are methane in addition to CO because these are detected when divided cell configuration along with the GDE is used.

Despite the slow diffusion process in solids, the small grain size in our electrodes supports diffusion, increasing faradaic efficiency for forming C3 products. The undivided cell's interface supplies active protons essential for CO_2ER. Acetone formation involves a C2–C3 coupling mechanism, where *COCHO species couple with *CO to form *CHOHCOCHO intermediates. The faradaic efficiency (FE) for CO production can drop to around 1%, indicating predominant C–C coupling in CO_2 interaction with the catalyst, yielding more complex products (Fig. 5e). This underscores the catalyst's preference for C–C coupling, yielding higher-order carbon compounds.

3.5 Electronic structure calculation using the DFT method

We employed the DFT method to calculate the formation of CO and CH_3COCH_3 *via* the CO_2ER process over the Cu_4 cluster supported on LSCO surfaces (the DFT calculation model is shown in Fig. S12†). The proposed reaction mechanism pathways are in the sequence of $CO_2 \rightarrow COOH^* \rightarrow CO \rightarrow COCO^* \rightarrow COCOH^* \rightarrow COCOCOH^* \rightarrow CHOCOCOH^* \rightarrow CHOHCOCOH^* \rightarrow CHOHCOCHOH^* \rightarrow CH_2OHCOCHOH^* \rightarrow CH_2COCHOH^* \rightarrow CH_2COCH_2OH \rightarrow CH_2COCH_2^* \rightarrow CH_2COCH_3^* \rightarrow CH_3COCH_3$. We have followed a similar mechanism to produce CO and CH_3COCH_3 *via* the CO_2ER process over nCu_4 (n = 3–5) clusters supported on LSCO surfaces. The free energy to produce CH_3COCH_3 on a $4Cu_4$ decorated LSCO surface (Fig. 6) was found to be more negative as compared to $3Cu_4$ + LSCO and $5Cu_4$ + LSCO surfaces, indicating it to be thermodynamically more
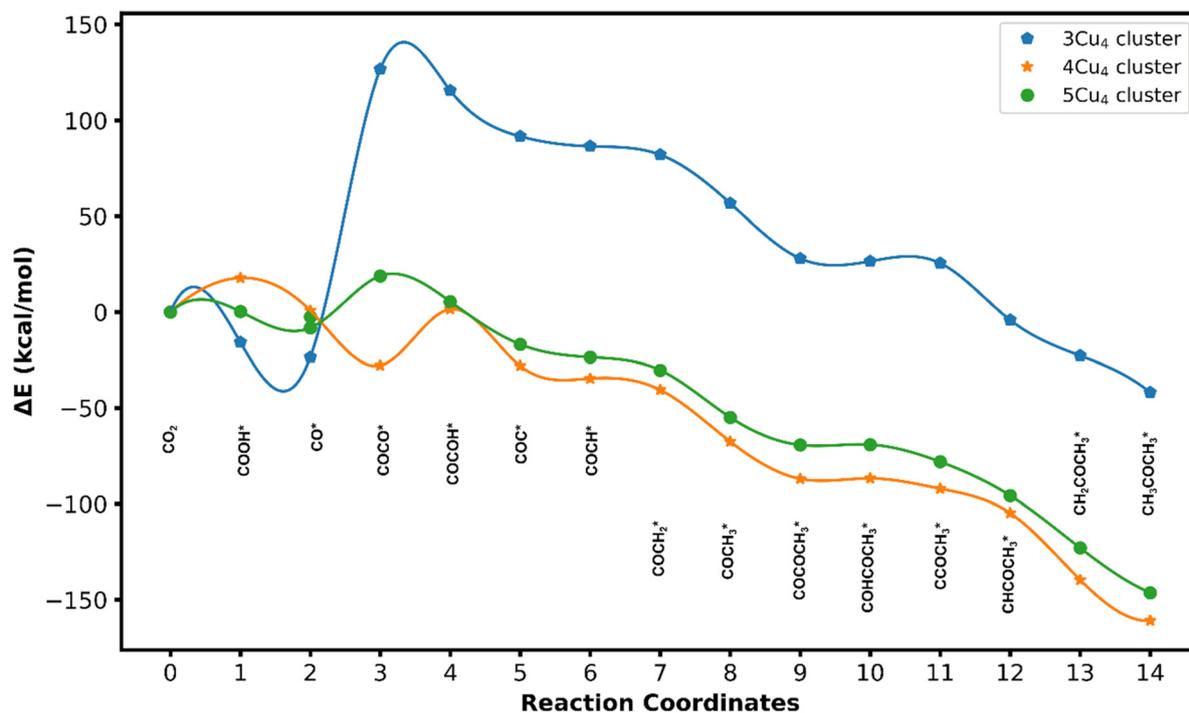
Fig. 6 A free energy diagram for the production of CH_3COCH_3 via CO_2ER on $3Cu_4 + LSCO$, $4Cu_4 + LSCO$ and $5Cu_4 + LSCO$ surfaces.

favourable under the CO_2ER process. In the initial step, CO_2 is reduced to form COOH* intermediate species followed by the single electron transfer pathway. Subsequently, the COOH* intermediate species is reduced, generating CO* species by reacting with a proton and releasing a H_2O molecule. The COCO* co-dimerization was crucial for the formation of C_2 products and responsible for the generation of the next intermediate species COCOH*. Our DFT study revealed that CO_2 can undergo facile conversion to adsorbed COCO* with a COOH* intermediate on the surfaces of $3Cu_4 + LSCO$, $4Cu_4 + LSCO$, and $5Cu_4 + LSCO$. However, we observed that the COCO* co-dimers are thermodynamically most stable on the $4Cu_4 + LSCO$ surface than the $3Cu_4 + LSCO$ and $5Cu_4 + LSCO$ surfaces. The free energy of the COCO* co-dimer in $4Cu_4 + LSCO$ (-22.89 kcal mol^{-1}) leads to the production of CH_3COCH_3, which is more thermodynamically lower than those of $3Cu_4 + LSCO$ (109.80 kcal mol^{-1}) and $5Cu_4 + LSCO$ (18.84 kcal mol^{-1}), respectively. In this study, the DFT investigation elucidates that altering the Cu_4 cluster decoration on the LSCO surface significantly influences the production of CH_3COCH_3. Out of these, the formation of CH_3COCH_3 is thermodynamically more stable on the $4Cu_4 + LSCO$ surface than in $3Cu_4 + LSCO$ and $5Cu_4 + LSCO$, respectively.

4. Conclusion

In conclusion, our investigation delves into the efficacy of Cu x/La$_{0.8}$Sr$_{0.2}$CoO$_3$ catalysts (Cu/LSCO) synthesized via solution combustion and chemical reduction methods for CO_2 electroreduction, with a particular emphasis on acetone pro-

duction, a process involving 16 electron transfers. Among the tested catalyst compositions, Cu 10/LSCO, Cu 20/LSCO, and Cu 30/LSCO displayed respective current densities of -11.36 mA cm^{-2}, -20.28 mA cm^{-2}, and -20.23 mA cm^{-2} under CO_2 purging conditions. Notably, Cu 20/LSCO exhibited a remarkable acetone formation of 93.7%, surpassing Cu 10/LSCO (39.9%) and Cu 30/LSCO (7.5%) in an undivided cell configuration. In contrast, significantly less catalytic current ($\sim$12 mA cm^{-2}) was observed in the H-cell configuration, where the products were primarily CO, CH_4, and H_2, with faradaic efficiencies of 4.3%, 1.6%, and 3.8%, respectively. Notably, acetone was not detected under these conditions. By increasing the electrode working area, the catalytic kinetics are enhanced, leading to measurable acetone formation ($\sim$3–4% faradaic efficiency) alongside smaller amounts of CO, CH_4, and H_2 (0.6%, 0.05%, and 1.3% faradaic efficiency, respectively). A comparative analysis between undivided and divided cell setups further highlights the advantage of the undivided configuration. The comparative differences in both the geometries are attributed to the distinct electrochemical environments in the two cell designs, emphasizing the role of cell configuration in product distribution. Clearly, acetone formation is a function of the design of the cell/electrode area and the metal–support interaction that one can attain by optimising these parameters.

Conflicts of interest

The authors declare no intellectual as well as financial conflict of interests.

Data availability

The data supporting the findings of this study are available within the article and its ESI.† All data analyzed during this study are available from the corresponding author upon request.

Acknowledgements

References

1 M. H. Eldesouki, A. E. Rashed and A. A. El-Moneim, *Clean Technol. Environ. Policy*, 2023, **25**, 3131–3148.

2 S. C. Peter, *ACS Energy Lett.*, 2018, **3**, 1557–1561.

3 G. Silvestri and O. Scialdone, *Carbon Dioxide as Chemical Feedstock*, John Wiley & Sons, Ltd, 2010, pp. 317–334.

4 O. S. Bushuyev, P. De Luna, C. T. Dinh, L. Tao, G. Saur, J. van de Lagemaat, S. O. Kelley and E. H. Sargent, *Joule*, 2018, **2**, 825–832.

5 S. She, J. Yu, W. Tang, Y. Zhu, Y. Chen, J. Sunarso, W. Zhou and Z. Shao, *ACS Appl. Mater. Interfaces*, 2018, **10**, 11715–11721.

6 Z. Han, X. Jia, X. Song, P. An, L. Fu, J. Yue, J. Yu, X. Liu, Z. Zhang, Y. Jin, M. He, D. Bai and G. Xu, *J. Cleaner Prod.*, 2023, **416**, 137943.

7 K. C. Poon, W. Y. Wan, H. Su and H. Sato, *RSC Adv.*, 2022, **12**, 22703–22721.

8 S. Overa, B. H. Ko, Y. Zhao and F. Jiao, *Acc. Chem. Res.*, 2022, **55**, 638–648.

9 P. Chen, Y. Zhang, Y. Zhou and F. Dong, *Nano Mater. Sci.*, 2021, **3**, 344–367.

10 S. Kaneco, N. Hiei, Y. Xing, H. Katsumata, H. Ohnishi, T. Suzuki and K. Ohta, *Electrochim. Acta*, 2002, **48**, 51–55.

11 J. Wu, Y. Huang, W. Ye and Y. Li, *Adv. Sci.*, 2017, **4**, 1700194.

12 C. Shi, K. Chan, J. S. Yoo and J. K. Nørskov, *Org. Process Res. Dev.*, 2016, **20**, 1424–1430.

13 W. Lai, Y. Qiao, Y. Wang and H. Huang, *Adv. Mater.*, 2023, **35**, 2306288.

14 M. Gattrell, N. Gupta and A. Co, *J. Electroanal. Chem.*, 2006, **594**, 1–19.

15 A. J. Garza, A. T. Bell and M. Head-Gordon, *ACS Catal.*, 2018, **8**, 1490–1499.

16 C. Wang, Z. Lv, X. Feng, W. Yang and B. Wang, *Adv. Energy Mater.*, 2023, **13**, 2302382.

17 Q. Chen, X. Wang, Y. Zhou, Y. Tan, H. Li, J. Fu and M. Liu, *Adv. Mater.*, 2024, **36**, 2303902.

18 X. Zhang, S.-X. Guo, K. A. Gandionco, A. M. Bond and J. Zhang, *Mater. Today Adv.*, 2020, **7**, 100074.

19 K. Zhao, X. Nie, H. Wang, S. Chen, X. Quan, H. Yu, W. Choi, G. Zhang, B. Kim and J. G. Chen, *Nat. Commun.*, 2020, **11**, 2455.

20 S. Dhakar and S. Sharma, *J. Phys. Chem. C*, 2024, **128**, 4862–4881.

21 J. Resasco, L. D. Chen, E. Clark, C. Tsai, C. Hahn, T. F. Jaramillo, K. Chan and A. T. Bell, *J. Am. Chem. Soc.*, 2017, **139**, 11277–11287.

22 S. W. Boettcher, S. Z. Oener, M. C. Lonergan, Y. Surendranath, S. Ardo, C. Brozek and P. A. Kempler, *ACS Energy Lett.*, 2021, **6**, 261–266.

23 B. Deng, M. Huang, X. Zhao, S. Mou and F. Dong, *ACS Catal.*, 2022, **12**, 331–362.

24 S. Chen, Y. Su, P. Deng, R. Qi, J. Zhu, J. Chen, Z. Wang, L. Zhou, X. Guo and B. Y. Xia, *ACS Catal.*, 2020, **10**, 4640–4646.

25 P. Saha, S. Amanullah and A. Dey, *Acc. Chem. Res.*, 2022, **55**, 134–144.

26 C.-T. Dinh, T. Burdyny, M. G. Kibria, A. Seifitokaldani, C. M. Gabardo, F. P. García de Arquer, A. Kiani, J. P. Edwards, P. De Luna, O. S. Bushuyev, C. Zou, R. Quintero-Bermudez, Y. Pang, D. Sinton and E. H. Sargent, *Science*, 2018, **360**, 783–787.

27 L. Wang, S. A. Nitopi, E. Bertheussen, M. Orazov, C. G. Morales-Guio, X. Liu, D. C. Higgins, K. Chan, J. K. Nørskov, C. Hahn and T. F. Jaramillo, *ACS Catal.*, 2018, **8**, 7445–7454.

28 G. Marcandalli, M. C. O. Monteiro, A. Goyal and M. T. M. Koper, *Acc. Chem. Res.*, 2022, **55**, 1900–1911.

29 Y. Hori, in *Modern Aspects of Electrochemistry*, ed. C. G. Vayenas, R. E. White and M. E. Gamboa-Aldeco, Springer, New York, NY, 2008, pp. 89–189.

30 X. Chen, L. Cavallo and K.-W. Huang, *ACS Catal.*, 2023, **13**, 13089–13100.

31 M. A. Abdel Rahim, R. M. Abdel Hameed and M. W. Khalil, *J. Power Sources*, 2004, **134**, 160–169.

32 S. Nellaiappan and S. Sharma, *ACS Appl. Energy Mater.*, 2019, **2**, 2998–3003.

33 Y. Zhou, A. J. Martín, F. Dattila, S. Xi, N. López, J. Pérez-Ramírez and B. S. Yeo, *Nat. Catal.*, 2022, **5**, 545–554.

34 K. P. Kuhl, E. R. Cave, D. N. Abram and T. F. Jaramillo, *Energy Environ. Sci.*, 2012, **5**, 7050–7059.

35 Y. Wang, L. Zhu, J. Li, W. Zhang, X. Shi, Y. Huang, M. Hojamberdiev and G. Zhu, *Adv. Powder Mater.*, 2023, **2**, 100119.

36 X. Qin, M. Chen, X. Chen, J. Zhang, X. Wang, J. Fang and C. Zhang, *ACS Appl. Nano Mater.*, 2022, **5**, 15574–15582.

37 A. Aitbekova, L. Wu, C. J. Wrasman, A. Boubnov, A. S. Hoffman, E. D. Goodman, S. R. Bare and M. Cargnello, *J. Am. Chem. Soc.*, 2018, **140**, 13736–13745.

38 A. Osti, L. Rizzato, J. Cavazzani, A. Meneghello and A. Glisenti, *Catalysts*, 2024, **14**, 313.

39 F. Wang, S. He, H. Chen, B. Wang, L. Zheng, M. Wei, D. G. Evans and X. Duan, *J. Am. Chem. Soc.*, 2016, **138**, 6298–6305.

40 S. Kattel, P. Liu and J. G. Chen, *J. Am. Chem. Soc.*, 2017, **139**, 9739–9754.

41 J. Chen, Y. Zhang, Z. Zhang, D. Hou, F. Bai, Y. Han, C. Zhang, Y. Zhang and J. Hu, *J. Mater. Chem. A*, 2023, **11**, 8540–8572.

42 S. Jayabal, G. Saranya, D. Geng, L.-Y. Lin and X. Meng, *J. Mater. Chem. A*, 2020, **8**, 9420–9446.

43 M. Xu, M. Peng, H. Tang, W. Zhou, B. Qiao and D. Ma, *J. Am. Chem. Soc.*, 2024, **146**, 2290–2307.

44 L. Liu and A. Corma, *Chem. Rev.*, 2018, **118**, 4981–5079.

45 A. Mohan and S. Sharma, *Electrochim. Acta*, 2024, **508**, 145218.

46 S. Royer, D. Duprez, F. Can, X. Courtois, C. Batiot-Dupeyrat, S. Laassiri and H. Alamdari, *Chem. Rev.*, 2014, **114**, 10292–10368.

47 D. Vyas, S. Dhakar, A. Singhal and S. Sharma, *Top. Catal.*, 2025, **68**, 346–356.

48 Q. Ji, L. Bi, J. Zhang, H. Cao and X. S. Zhao, *Energy Environ. Sci.*, 2020, **13**, 1408–1428.

49 M. A. Peña and J. L. G. Fierro, *Chem. Rev.*, 2001, **101**, 1981–2018.

50 E. Gazzarrini, K. Rossi and F. Baletto, *Nanoscale*, 2021, **13**, 5857–5867.

51 N. Dutta, D. Bagchi, G. Chawla and S. C. Peter, *ACS Energy Lett.*, 2024, **9**, 323–328.

52 B. Ravel and M. Newville, *J. Synchrotron Radiat.*, 2005, **12**, 537–541.

53 B. Ravel, *J. Synchrotron Radiat.*, 2001, **8**, 314–316.

54 B. Liu, X. Yao, Z. Zhang, C. Li, J. Zhang, P. Wang, J. Zhao, Y. Guo, J. Sun and C. Zhao, *ACS Appl. Mater. Interfaces*, 2021, **13**, 39165–39177.

55 S. Dhakar, J. Nama, V. Kumari, R. Khatua, A. Mondal and S. Sharma, *Electrochim. Acta*, 2023, **441**, 141791.

56 S. Dhakar, S. Mukhopadhyay, M. Ottakam Thotiyl and S. Sharma, *J. Colloid Interface Sci.*, 2024, **654**, 688–697.

57 A. C. Lazanas and M. I. Prodromidis, *ACS Meas. Sci. Au*, 2023, **3**, 162–193.

58 A. Sacco, *J. CO2 Util.*, 2018, **27**, 22–31.

59 Y. Li, Y. Zhang, L. Shi, X. Liu, Z. Zhang, M. Xie, Y. Dong, H. Jiang, Y. Zhu and J. Zhu, *Small*, 2024, 2402823.

60 Y. Li, F. Liu, Z. Chen, L. Shi, Z. Zhang, Y. Gong, Y. Zhang, X. Tian, Y. Zhang, X. Qiu, X. Ding, X. Bai, H. Jiang, Y. Zhu and J. Zhu, *Adv. Mater.*, 2022, **34**, 2206002.

61 G. Dong, G. Wang, J. Cheng, M. Li, Z. Liang, D. Geng and W. Tang, *Appl. Catal., B*, 2024, **342**, 123444.

62 C. Lucky and M. Schreier, *ACS Nano*, 2024, **18**, 6008–6015.

63 Y. Hori, A. Murata and R. Takahashi, *J. Chem. Soc., Faraday Trans. 1*, 1989, **85**, 2309–2326.

64 C. Ampelli, F. Tavella, D. Giusi, A. M. Ronsisvalle, S. Perathoner and G. Centi, *Catal. Today*, 2023, **421**, 114217.

65 J. Liu, P. Li, J. Bi, S. Jia, Y. Wang, X. Kang, X. Sun, Q. Zhu and B. Han, *J. Am. Chem. Soc.*, 2023, **145**, 23037–23047.

66 W. Xia, Y. Xie, S. Jia, S. Han, R. Qi, T. Chen, X. Xing, T. Yao, D. Zhou, X. Dong, J. Zhai, J. Li, J. He, D. Jiang, Y. Yamauchi, M. He, H. Wu and B. Han, *J. Am. Chem. Soc.*, 2023, **145**, 17253–17264.

67 Y. Sun, J. Xie, Z. Fu, H. Zhang, Y. Yao, Y. Zhou, X. Wang, S. Wang, X. Gao, Z. Tang, S. Li, X. Wang, K. Nie, Z. Yang and Y.-M. Yan, *ACS Nano*, 2023, **17**, 13974–13984.

68 J. Feng, L. Wu, S. Liu, L. Xu, X. Song, L. Zhang, Q. Zhu, X. Kang, X. Sun and B. Han, *J. Am. Chem. Soc.*, 2023, **145**, 9857–9866.